Applied Catalysis B: Environment and Energy 383 (2026) 126069

Contents lists available at ScienceDirect

Applied Catalysis B: Environment and Energy

journal homepage: www.elsevier.com/locate/apcatb

Activating Ni via heterostructure-induced electron deficiency and spatial intermediate coupling for enhanced alkaline HER/HOR

Wanli Liang [a,b], Zixuan Dan [b], Xiyu Gong [b], Jinchang Xu [b,c], Hongjuan Wang [a], Yonghai Cao [a], Hao Yu [a], Yanshuo Jin [b,*], Hao-Fan Wang [a,*]

[a] School of Chemistry and Chemical Engineering, Guangdong Provincial Key Lab of Green Chemical Product Technology, South China University of Technology, Guangzhou 510641, China
[b] Siyuan Laboratory, Guangzhou Key Laboratory of Vacuum Coating Technologies and New Energy Materials, Guangdong Provincial Engineering Technology Research Center of Vacuum Coating Technologies and New Energy Materials, Guangdong Provincial Key Laboratory of Nanophotonic Manipulation, Department of Physics, Jinan University, Guangzhou 510632, China
[c] GBA Branch of Aerospace Information Research Institute, Chinese Academy of Sciences, Guangzhou 510700, China

ARTICLE INFO

Keywords:
Helmholtz layer
Hydrogen catalysis
Ni/WN interface
Intermediate adsorption
Volmer kinetics

ABSTRACT

The development of hydrogen energy conversion technology offers a solution to the global energy crisis. Hydrogen evolution reaction (HER) and hydrogen oxidation reaction (HOR) are essential for hydrogen production and utilization. Ni-based catalysts are promising alternatives to Pt-group catalysts under alkaline conditions. However, pure Ni exhibits low activity due to H_2O dissociation/formation limitations in the rate-determining Volmer step. To overcome this bottleneck, we present a heterostructure-induced electron modulation strategy to regulate the spatial proximity of key intermediates within the inner Helmholtz plane, thereby facilitating Volmer step kinetics. Electron depletion at the Ni site shifts its *d*-band center upward, enhancing the adsorption of *H, *OH, and *H_2O. This electronic tuning brings *H and *OH closer and elongates the H–OH bonds in *H_2O, effectively reducing the Volmer barrier, as confirmed by density functional theory (DFT) and *in-situ* Raman spectroscopy. We demonstrate this concept using a representative heterostructure of nickel and tungsten nitride on nickel foam (Ni/WN@NF), which exhibits excellent electrocatalytic activity, requiring only 20 mV overpotential to achieve 10 mA cm^{-2} for HER and reaching an exchange current density of 3.99 mA cm^{-2} for HOR. This work offers a generalizable interfacial approach for modulating local chemical environments in alkaline hydrogen electrocatalysis.

1. Introduction

The excessive reliance on fossil fuels has caused significant environmental degradation, intensifying the global demand for clean, renewable energy sources. Hydrogen stands out as a promising alternative due to its high gravimetric energy density and water as the sole byproduct in fuel cells [1]. In the context of hydrogen production and conversion, hydrogen evolution reaction (HER) and hydrogen oxidation reaction (HOR) are fundamental to enabling water electrolysis and fuel cells for clean energy [2,3]. While platinum group metals (PGMs) demonstrate high activity in acidic media, their high cost and scarcity restrict large-scale application [4,5]. Alkaline systems offer an opportunity to replace PGMs with earth-abundant materials such as nickel [2]. Nevertheless, pure Ni exhibits sluggish HER and HOR kinetics, primarily due to its strong *H binding and insufficient *OH adsorption, which together hinder the key Volmer step involving water dissociation and formation [6–8].

To overcome the intrinsic limitations of pure Ni, various heterostructures such as Ni/NiO/C [9], Ni/MoO_{2-x} [10], Ni/V_2O_3 [11], and Ni_3N/Ni [12] have been explored to optimize adsorption of key intermediates, especially the Gibbs free energies of adsorbed H and OH species (ΔG_{H^*} and ΔG_{OH^*}). These designs have significantly improved the HER and HOR performances by optimizing the thermodynamic binding affinities of *H and *OH. However, most efforts to date have centered on thermodynamic descriptors, often neglecting the kinetic constraints that control reaction rates under alkaline conditions. In particular, the Volmer step, involving water dissociation or recombination, is widely recognized as the rate-determining step in both HER

* Corresponding authors.
E-mail addresses: jinyanshuo@email.jnu.edu.cn (Y. Jin), whf@scut.edu.cn (H.-F. Wang).

https://doi.org/10.1016/j.apcatb.2025.126069
Received 26 July 2025; Received in revised form 25 September 2025; Accepted 10 October 2025
Available online 11 October 2025
0926-3373/© 2025 Elsevier B.V. All rights are reserved, including those for text and data mining, AI training, and similar technologies.

and HOR. This step occurs within the Helmholtz layer at the electrode-electrolyte interface, where the interaction strength and spatial proximity of *H, *OH, and *H_2O have a critical impact on the energy barrier [13,14]. However, how the intermediate adsorption strength affects the spatial arrangement and catalytic reactivity in the Helmholtz layer remains an underexplored frontier in alkaline HER/-HOR catalysis.

Herein, we report a strategy that employs a nickel-tungsten nitride (Ni/WN) heterostructure to modulate the Helmholtz layer via heterostructure-induced electron deficiency. Spectroscopic characterization and charge density analysis confirm spontaneous electron transfer from Ni to WN, resulting in an upward shift of the Ni *d*-band center. This electronic modulation enhances the adsorption strength of the intermediates and reduces their spatial distance to the Ni active sites. The resulting Ni/WN@NF delivers excellent bifunctional activity in alkaline media. KSCN poisoning experiments verify that Ni serves as the active center for hydrogen electrocatalysis. Compared to pure Ni@NF, Ni/WN@NF exhibits a low HER Tafel slope of 49 mV dec^{-1} and a 5.5-fold increase in HOR exchange current density. *In-situ* Raman spectroscopy and density functional theory (DFT) calculations further reveal that electron-deficient Ni strengthens interactions with *H, *OH, and *H_2O in the Helmholtz layer, bringing *H and *OH closer together and elongating the H–OH bond of *H_2O, thereby reducing the energy barrier of the Volmer step. These findings provide a promising approach for Helmholtz layer modulation and offer mechanistic insights for designing efficient alkaline HER/HOR electrocatalysts.

2. Experimental section

2.1. Materials

Ammonium metatungstate [$(NH_4)_6H_2W_{12}O_{40}{\cdot}x\ H_2O$, 99.5 % metals basis], Nickel nitrate hexahydrate [$Ni(NO_3)_2{\cdot}6\ H_2O$, 98 %], and tungsten (W, 99.9 % metals basis, 50 nm) were purchased from Shanghai Aladdin Biochemical Technology Co., Ltd. Nickel chloride ($NiCl_2{\cdot}6\ H_2O$, A.R.) was obtained from Tianjin Damao Chemical Reagent Factory. Urea (CH_4N_2O, 99 %), potassium hydroxide (KOH, 95 %), and ethanol (C_2H_6O, AR, 99.7 %) were acquired from Shanghai Macklin Biochemical Technology Co., Ltd. Hydrochloric acid (HCl, G.R.) was obtained from Guangzhou Chemical Reagent Factory. Nickel foam (1.0 nm) was supplied by Kunshan Jiayisheng Electronics Co., Ltd. Pt/C (commercially available Johnson Matthey Hispec4000 catalyst, nominal Pt content of 40 wt%) and Nafion (DuPont D520, 5 %) were purchased from Shanghai Hesen Electric Co., Ltd. The water throughout the experiments was purified using an ultrapure water system.

2.2. Synthesis of Ni/WN catalyst

First, a piece of nickel foam (NF) measuring 2 cm × 4 cm was immersed in an HCl solution for 20 min to remove the surface oxide layer and then rinsed thoroughly with deionized water. Separately, 70 mmol/L $(NH_4)_6H_2W_{12}O_{40}{\cdot}x\ H_2O$ and 100 mmol/L $Ni(NO_3)_2{\cdot}6\ H_2O$ were dissolved in 30 mL of deionized water to form a homogeneous solution. The cleaned NF and the solution were transferred into a 50 mL Teflon-lined hydrothermal reactor together and heated at 180°C for 12 h in an electric thermostatic oven. After cooling to room temperature, the precursor-loaded NF was rinsed with deionized water and dried at 60°C, yielding the NiWO@NF-pre sample. Finally, the NiWO@NF-pre was placed in a tube furnace and annealed at 600°C for 1 h in an N_2 atmosphere (denoted as NiWO@NF) and then further annealed at 550°C for 3 h in an NH_3 atmosphere to obtain the Ni/WN@NF electrode. The catalyst loading of Ni/WN@NF was approximately 150 mg cm^{-2}.

To investigate the effect of $Ni(NO_3)_2{\cdot}6\ H_2O$ concentration, Ni/WN@NF-0, Ni/WN@NF-50, and Ni/WN@NF-150 were synthesized using 0, 50, and 150 mmol/L of $Ni(NO_3)_2{\cdot}6\ H_2O$ in the solution, respectively. To study the influence of NH_3 annealing time, the samples were annealed at 550°C for 0, 1, and 6 h. The resulting products were named Ni/WN@NF-0h, Ni/WN@NF-1h, and Ni/WN@NF-6h, respectively. Furthermore, Ni/WN@CP was synthesized by introducing two pieces of carbon paper (CP) with a size of 2 cm × 4 cm during the hydrothermal reaction, followed by the same annealing process.

2.3. Synthesis of Ni@NF

The synthesis of Ni@NF was based on previous reports [15,16]. Two pieces of NF (1 cm ×1 cm) were first cleaned with HCl solution and rinsed with deionized water. Then, 200 mg of $NiCl_2{\cdot}6\ H_2O$ and 200 mg of CH_4N_2O were dissolved in 30 mL of deionized water. The solution and NF were transferred to a 50 mL Teflon reactor, heated to 150°C in an oven, and maintained for 12 h. After cooling, the NF with precursors was rinsed with deionized water and dried. Finally, it was annealed at 450°C for 1 h in an H_2 atmosphere to obtain Ni@NF.

2.4. Synthesis of WN

Commercial tungsten powder was first oxidized by heating to 600°C in air for 1 h. The obtained material was then heated to 800°C in an NH_3 atmosphere a for 2 h to obtain WN.

2.5. Characterizations

The X-ray diffraction (XRD) patterns were obtained using a Rigaku *Miniflex 600*, with a scanning step of 0.01° and a sampling interval of 0.05 s. Raman spectra were recorded using a Zolix *RTS-Mini* Raman spectrometer with a 532 nm excitation wavelength. Scanning electron microscopy (SEM) images was obtained using a *Regulus 8230* high-resolution cold field emission scanning electron microscope at an accelerating voltage of 5 kV. High-resolution transmission electron microscope (HRTEM) images were captured using a *JEOL JEM 2100 F*, equipped with an Oxford energy dispersive spectrometer (EDS). X-ray photoelectron spectroscopy (XPS) data were acquired on a Thermo Fisher Scientific K-Alpha, with data calibrated to the C 1 *s* peak at 284.80 eV. X-ray absorption near-edge structure (XANES) and extended X-ray absorption fine structure (EXAFS) data were collected in transmission mode at *SPring-8* (Super Photon ring-8).

In-situ Raman spectroscopy was performed using a 300 nm Ag substrate (loaded with 1 mg cm^{-2}) for surface-enhanced Raman spectra [17]. The measurements were performed with the following parameters: laser wavelength of 532 nm, laser power set to 2.450 mW (measured with an optical power meter, Thorlab PM400K3), a 50 × objective lens (Soptop, NA = 0.55, WD = 7.9), exposure time of 30 s, and a potential step interval of 100 mV. The broad O–H peak of water in the range of 3000–3800 cm^{-1} was deconvoluted into three components using Gaussian fitting in Origin software. The three components correspond to different hydrogen-bonded water structures: 4-HB·H_2O (3211 cm^{-1}), 2-HB·H_2O (3430 cm^{-1}), and $K^+{\cdot}H_2O$ (3607 cm^{-1}) [18]. The half-peak widths of the 4-HB·H_2O, 2-HB·H_2O, and $K^+{\cdot}H_2O$ bands were 150 cm^{-1}, 250 cm^{-1}, and 150 cm^{-1}, respectively [19].

2.6. Preparation of WN@NF and Pt/C@NF electrodes

The material was dispersed in ethanol containing 5 % Nafion via ultrasonication to form a slurry. The slurry was then applied to the surface of NF and allowed to dry naturally to prepare the corresponding electrode.

2.7. Electrochemical measurements

Electrochemical performance was measured using a Bio-Logic multichannel electrochemical workstation in a standard three-electrode system. The working electrode was a piece of NF (0.5 cm × 0.5 cm) loaded with the catalyst. The reference electrode was a Hg/HgO electrode,

calibrated by the open circuit potential of Pt/C in an H_2-saturated electrolyte, and the counter electrode was a carbon rod.

HER performance was evaluated in 1 M KOH. Polarization curves were obtained using cyclic voltammetry at a scan rate of 1 mV s^{-1} with *iR* correction for solution resistance. Nyquist plots were acquired using electrochemical impedance spectroscopy (EIS) at −100 mV vs. RHE over a frequency range of 200 kHz to 10 mHz. Stability tests were conducted by recording potential–time curves at 10 and 100 mA cm^{-2} using the chronpotentiometry method.

HOR tests were conducted in 0.1 M KOH saturated with H_2. Steady-state polarization curves were obtained using chronoamperometry, holding each potential for 3 min to record the current response. Stability was assessed by recording current-time curve at 0.1 V vs. RHE.

2.8. Calculation methods

Spin-polarized density functional theory calculations were conducted using the Vienna Ab-initio Simulation Package (VASP) [20,21] to study HOR processes on prepared surfaces. The Projector augmented wave (PAW) [21] method with a cutoff energy of 400 eV and the Perdew-Burke-Ernzerhof (PBE) functional [22] were employed in these calculations. The DFT-D3 method [23] was applied to account for van der Waals interactions. Surface models were constructed with three layers of WN (111) and four layers of Ni (111), separated by a 15 Å vacuum layer, while half of the bottom atomic layers were fixed to simulate the bulk phase. For the Ni/WN heterostructure, two layers of Ni (111) facets were placed on two layers of WN (111) facets, with the bottom three atomic layers fixed. All models were relaxed to meet an energy convergence criterion of 10^{-5} eV and a force convergence criterion of 0.02 eV $Å^{-1}$. The Brillouin zone was sampled using a K-point mesh of 0.04 × 2π $Å^{-1}$. To calculate the energy barriers for the water formation process on the Ni and Ni/WN surfaces, constrained ab initio molecular dynamics (AIMD) with the slow growth method was employed. The collective variable was defined as the distance between the H atom and the O atom, which was incrementally increase by 0.001 Å per MD step. The adsorption energies (E_{ads}) were calculated as

$$E_{ads} = E_{total} - E_{substrate} - E_{adsorbate} \quad (1)$$

where E_{total}, $E_{substrate}$, and $E_{adsorbate}$ represent the energy of the adsorbed structure, substrate, and adsorbate, respectively. The free energies were calculated using the following formula:

$$G = E_{DFT} + ZPE - TS \quad (2)$$

the *G*, E_{DFT}, *ZPE*, and *TS* represent the free energy, energy from DFT calculations, zero-point energy, and entropic contribution, respectively.

3. Result and discussion

3.1. Synthesis and characterization of Ni/WN@NF

The construction of Ni-based heterostructures allows modulation of the electronic density at Ni sites, thereby optimizing the adsorption of key intermediates and enhancing HER/HOR activity. As illustrated in Fig. S1a, a comparison is made between electron-enriched and electron-depleted Ni sites. Electron-rich Ni shifts the *d*-band center downward, whereas electron-poor Ni shifts it upward, which enhances the adsorption of key intermediates according to the *d*-band center theory [24,25]. Based on the position of metallic Ni in the three-dimensional volcano plot (Fig. S1b and S2–S4), water dissociation is the rate-limiting step, and insufficient *OH adsorption limits the alkaline HER/HOR activity [8]. For Ni catalysts in alkaline media, the *OH binding strength plays a dominant role [26,27]. If surface adsorption weakens, *OH adsorption further deviates from the optimal activity region. Therefore, in this work, the Ni-based heterostructure is designed to induce electron deficiency at Ni sites, enhancing the adsorption of key intermediates and further investigating their role in the water dissociation/formation energy barrier and catalytic performance.

The schematic diagram in Fig. 1a illustrates the synthesis method of the representative Ni/WN heterostructure supported by nickel foam (Ni/WN@NF). Initially, a precursor of Ni and W oxides (NiWO@NF-pre) was synthesized via a hydrothermal reaction involving nickel foam in a solution of ammonium metatungstate [$(NH_4)_6H_2W_{12}O_{40}{\cdot}x\ H_2O$] and nickel nitrate [$Ni(NO_3)_2{\cdot}6\ H_2O$], where NF served as both the support and a partial source of Ni [28,29]. The NiWO@NF-pre was then subjected to sequential annealing in N_2 and NH_3 atmospheres to obtain Ni/WN@NF. The microstructure of the samples was examined using SEM and transmission electron microscopy (TEM). Substantial growth of nanowires was observed on the NF surface during the hydrothermal reaction, and this nanowire morphology was preserved through the annealing process (Fig. 1b, c and S5–S6).

The structure and crystalline phase of the Ni/WN heterostructure were characterized by XRD. The XRD pattern of Ni/WN@NF (Fig. 1d and S7) shows sharp peaks at 43.9°, 51.4°, and 75.7°, corresponding to cubic Ni (111), (200), and (220) planes, likely originating from NF. Additionally, diffraction peaks at 36.9°, 43.3°, 62.8°, and 75.7° are attributed to the (111), (200), (220), and (311) crystal planes of cubic WN (PDF#75–1012), confirming the presence of tungsten nitride. To further clarify the structure, Ni/WN was exfoliated from the NF by sonication. Notably, the peak at 51.8° in the XRD pattern of Ni/WN (Fig. S8 and S9) is indexed as cubic Ni (PDF#04–0850), indicating the presence of Ni and further corroborating that Ni/WN is a heterostructure of nickel and tungsten nitride. In contrast, obtained by the annealing of NiWO@NF-pre only in N_2 atmosphere, the NiWO@NF is composed of triclinic WO_3 (PDF#32–1395) and cubic Ni (PDF#04–0850). It is posited that during the NH_3 annealing process, lattice oxygen in WO_3 is replaced by nitrogen in NH_3, leading to the formation of tungsten nitride [30]. The composition of Ni/WN@NF was further confirmed by XPS. Specifically, the appearance of the N 1 *s* signal in the XPS survey spectra (Fig. S10), the decreased O: W ratio (Table S1), and the presence of characteristic W–N peaks [31,32] in the W 4 *f* XPS spectrum (Fig. S11) support the formation of tungsten nitride. Importantly, with the transformation from tungsten oxide to tungsten nitride, significant improvements in HER and HOR electrocatalytic activities were observed (Fig. S12–S15 and Table S2).

To further confirm the structure of Ni/WN, selected area electron diffraction (SAED) was conducted. The obtained pattern displays distinct diffraction spots corresponding to the Ni (111), (200), and (220) planes, as well as the WN (111), (200), (220), and (311) planes (Fig. S16). The uniform distribution of Ni, W, and N elements in the EDS mapping images indicates the presence of numerous Ni/WN interfaces (Fig. 1e–h). HRTEM image revealed interplanar spacings of 1.85 and 2.39 Å, corresponding to the Ni (200) and WN (111) crystal planes (Fig. 1i–k). To better describe the Ni/WN interface, separate Ni@NF (Fig. S17–S21) and WN (Fig. S17 and S22–24) samples were used for comparison. Raman spectroscopy analysis (Fig. S25) was conducted to investigate possible different vibration modes in these samples. The four similar peaks at 253, 321, 703, and 810 cm^{-1} suggest that N and O may exist in similar states in the Ni/WN and WN lattices [33–35]. Additionally, a peak related to Ni–O scattering was observed at a higher Raman shift (898 cm^{-1}), attributed to O species on the Ni surface [35,36].

3.2. Electronic structure of Ni/WN

Density functional theory calculations and spectroscopic analyses are employed to further probe the coordination structure and electronic environment of the Ni/WN heterostructure. Models of Ni, WN, and Ni/WN were constructed in Fig. S2 and S26. The projected density of states (PDOS) in Fig. 2a reveals that both Ni and WN are metallic, with differences in their electronic density of states at the Fermi level [37,38]. The work functions of Ni@NF and WN were assessed using XPS. As

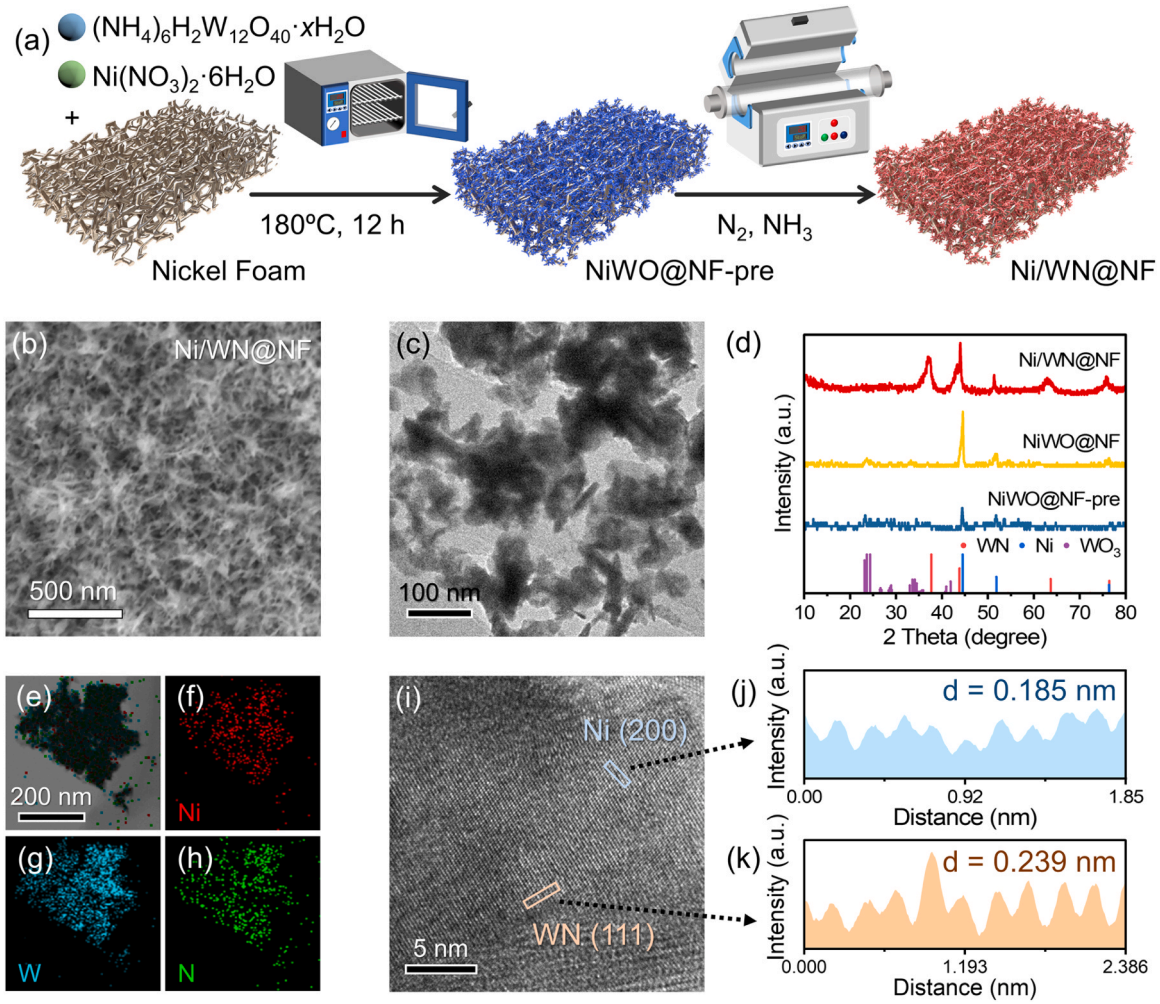

Fig. 1. Synthesis and characterization of Ni/WN@NF. (a) Schematic diagram of the synthesis of Ni/WN@NF. (b) SEM image of Ni/WN@NF. (c) TEM image of Ni/WN. (d) XRD patterns of NiWO@NF-pre, NiWO@NF, and Ni/WN@NF. (e) HAADF-STEM image and EDS mappings of (f) Ni, (g) W, and (h) N in the Ni/WN. (i) HRTEM image of Ni/WN. The lattice spacing distributions of (j) Ni (200) and (k) WN (111) in Ni/WN correspond to the box from top to bottom in the HRTEM image.

shown in Fig. 2b, the work function of Ni@NF (4.15 eV) is lower than that of WN (4.47 eV). When in close contact, the different work functions may induce a built-in electric field, leading to spontaneous electron transfer from Ni to WN, as illustrated in Fig. 2c [39].

Accordingly, X-ray absorption spectroscopy (XAS) is conducted to probe the influence of the heterostructure on the local coordination and electronic structure of Ni. Fig. 2d presents the XANES spectra of Ni/WN, Ref-Ni, and Ref-NiO at the Ni K-edge. Compared with Ref-Ni, the pre-edge of Ni/WN shifts to higher energy values, indicating a lower average electron density near the Ni site than in metallic Ni. Fourier transform extended X-ray absorption fine structure (FT-EXAFS) results (Fig. 2e) show that the first shell layer of Ni/WN mainly contains a Ni–Ni coordination peak (~2.15 Å), similar to the *R* spatial distribution of metallic Ni but different from that of NiO. The *k*-space (Fig. S27) and wavelet transform (WT) plots (Fig. 2f) of EXAFS further demonstrate the similar coordination environments between Ni/WN and Ref-Ni, corroborating the presence of a metallic Ni phase in Ni/WN. The Ni K-edge EXAFS fitting results (Fig. S28 and Table S3) of Ref-Ni and Ni/WN show that in Ni/WN, the Ni–Ni coordination number is reduced to 5.27, while a Ni–N coordination number of 1.71 is observed, indicating extensive Ni–WN bonding and the formation of abundant interfacial structures within the heterostructure.

From the W L_3-edge XANES spectra (Fig. 2g), the intensity of the white line of Ni/WN is lower than that of Ref-WO_3, indicating that the oxidation state of W in Ni/WN is lower than in WO_3, supporting the reduction of W during the conversion of tungsten oxide to tungsten nitride. FT-EXAFS spectra (Fig. 2h) show that the coordination peak attributed to W–N in the first shell of Ni/WN (~1.44 Å) is similar to that of W–O (~1.38 Å), while the W–N–W scattering pattern (~3.10 Å) in the second shell differs from that of W–O–W [34,40]. Additionally, WT plots of Ni/WN and Ref-WO_3 (Fig. S29 and S30) reveal the maximum intensities located at 6.0 $Å^{-1}$ and 8.3 $Å^{-1}$, respectively, corresponding to W–N and W–O coordination. In summary, a heterostructure of metallic Ni and tungsten nitride was constructed, in which Ni exists in a metallic form with a lower electron density than typical metallic Ni.

The surface charge distribution plays a crucial role in influencing the electrocatalytic activity of HER and HOR. To further explore the electronic states of the surfaces, XPS was used to obtain the elemental chemical states of Ni/WN@NF, WN, and Ni@NF (Fig. S31). The XPS spectra of Ni 2 *p* are shown in Fig. 3a. The Ni 2 *p* XPS spectrum of Ni/WN@NF is split into four groups of double peaks. The peaks at 853.22 and 870.38 eV are attributed to Ni^0 $2p_{3/2}$ and Ni^0 $2p_{1/2}$, respectively [41,42]. The peaks at 856.29/858.25 and 874.06/876.28 eV correspond to Ni $2p_{3/2}$ and Ni $2p_{1/2}$ of Ni^{2+}/Ni^{3+}, respectively, likely due to the slight surface oxidation, with two satellite peaks observed at 861.95 and 880.36 eV [41,43]. Crucially, compared with Ni@NF, the peaks of Ni^{2+} $2p_{3/2}$ and Ni^{2+} $2p_{1/2}$ in Ni/WN@NF are positively shifted by 1.37 and 1.28 eV, respectively, indicating electron loss at the Ni site at the Ni/WN interface.

For the W 4 *f* XPS spectrum of Ni/WN@NF (Fig. 3b), the peaks at

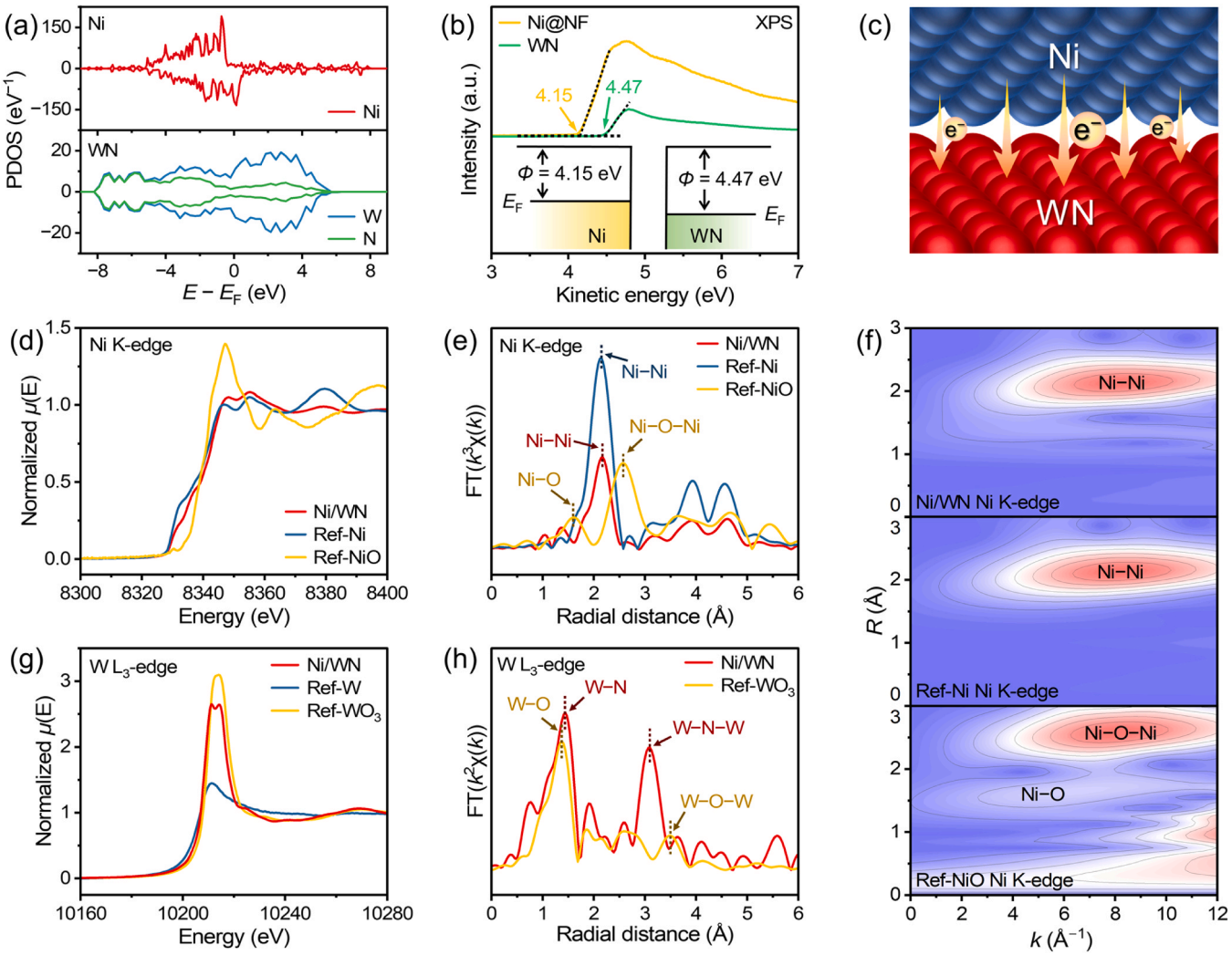

Fig. 2. Chemical environment of Ni/WN heterostructure. (a) Projected density of states (PDOS) of Ni and WN. (b) Secondary electron cutoff XPS spectra of Ni and WN, and the inset is the energy band diagram of Ni and WN. (c) Schematic diagram of charge transfer at the interface between metal Ni and tungsten nitride. (d) Ni K-edge XANES spectra of Ni/WN, Ref-Ni, and Ref-NiO. (e) FT-EXAFS spectra of Ni/WN, Ref-Ni, and Ref-NiO. (f) Wavelet transform (WT) plots for k^3-weighted Ni K-edge EXAFS signal of Ni/WN, Ref-Ni, and Ref-NiO. (g) W L_3-edge XANES spectra of Ni/WN, Ref-W, Ref-WO_3. (h) FT-EXAFS spectra of Ni/WN and Ref-WO_3.

33.04 and 35.16 eV can be assigned to the W $4f_{7/2}$ and W $4f_{5/2}$ orbitals of W–N, confirming the presence of tungsten nitride [31,32]. Additionally, the peaks at 35.59 and 37.74 eV are attributed to W–O, possibly due to surface oxidation of W [32]. In the N 1 *s* XPS spectrum of Ni/WN@NF (Fig. 3c), the peak at the lowest binding energy (397.44 eV) is associated with the N–W bond, while the peaks at 399.75 and 401.91 eV are related to N–C and N–O bonds, respectively [31,32,40]. Notably, the binding energies of the W 4 *f* and N 1 *s* peaks of Ni/WN@NF are negatively shifted compared with those of WN, suggesting that tungsten nitride in the Ni/WN heterostructure has a higher electron density. These results indicate electron transfer from Ni to WN at the Ni/WN heterointerface.

Moreover, the electronic structure of the Ni/WN heterostructure was analyzed by DFT calculation. Compared with metallic Ni (Fig. 2a), the Ni/WN heterostructure (Fig. 3d) exhibits increased electron density at the Fermi level, indicating that the formation of a heterostructure with WN can enhance the electrical conductivity of Ni [44]. Charge density difference analysis is an effective strategy for investigating electron transfer behavior, with simulation results presented in Fig. 3e. In the optimized three-dimensional atomic model, the cyan area on the Ni side represents charge depletion, while the yellow area on the WN side represents charge accumulation. The corresponding curve further demonstrates charge loss at the Ni site and charge enrichment on the WN side, supporting the hypothesis of charge transfer from Ni to WN [37,38]. Bader charge analysis reveals that Ni transfers 3.26 e^- to WN (Fig. 3f), highlighting the strong electronic coupling at the heterointerface.

It is noteworthy that the electron deficiency at the Ni site results in an elevation of the *d*-band center relative to the Fermi level to maintain a fixed *d* orbital occupancy, as illustrated in Fig. 3g. Additionally, the electronic structure of Ni in the *d* orbitals of Ni and Ni/WN was examined via DFT calculations (Fig. 3h and 3i). The PDOS reveals that the spin-up *d*-band center of Ni in Ni/WN (−1.48 eV) shifts closer to the Fermi level compared to pure Ni (−1.72 eV). This shift is expected to enhance the adsorption of *H, *OH, and *H_2O, leading to the regulation of H–OH in the inner Helmholtz layer, thereby facilitating the formation/dissociation steps of *H_2O and improving the kinetics of alkaline HER/HOR.

3.3. HER/HOR performance of Ni/WN@NF

The alkaline HER electrocatalytic performance of the Ni/WN@NF electrode was investigated in a 1 M KOH solution. The polarization curves (Fig. 4a) reveal that Ni/WN@NF exhibits a low overpotential of 20 mV at 10 mA cm^{-2}, slightly higher than that of Pt/C@NF (15 mV)

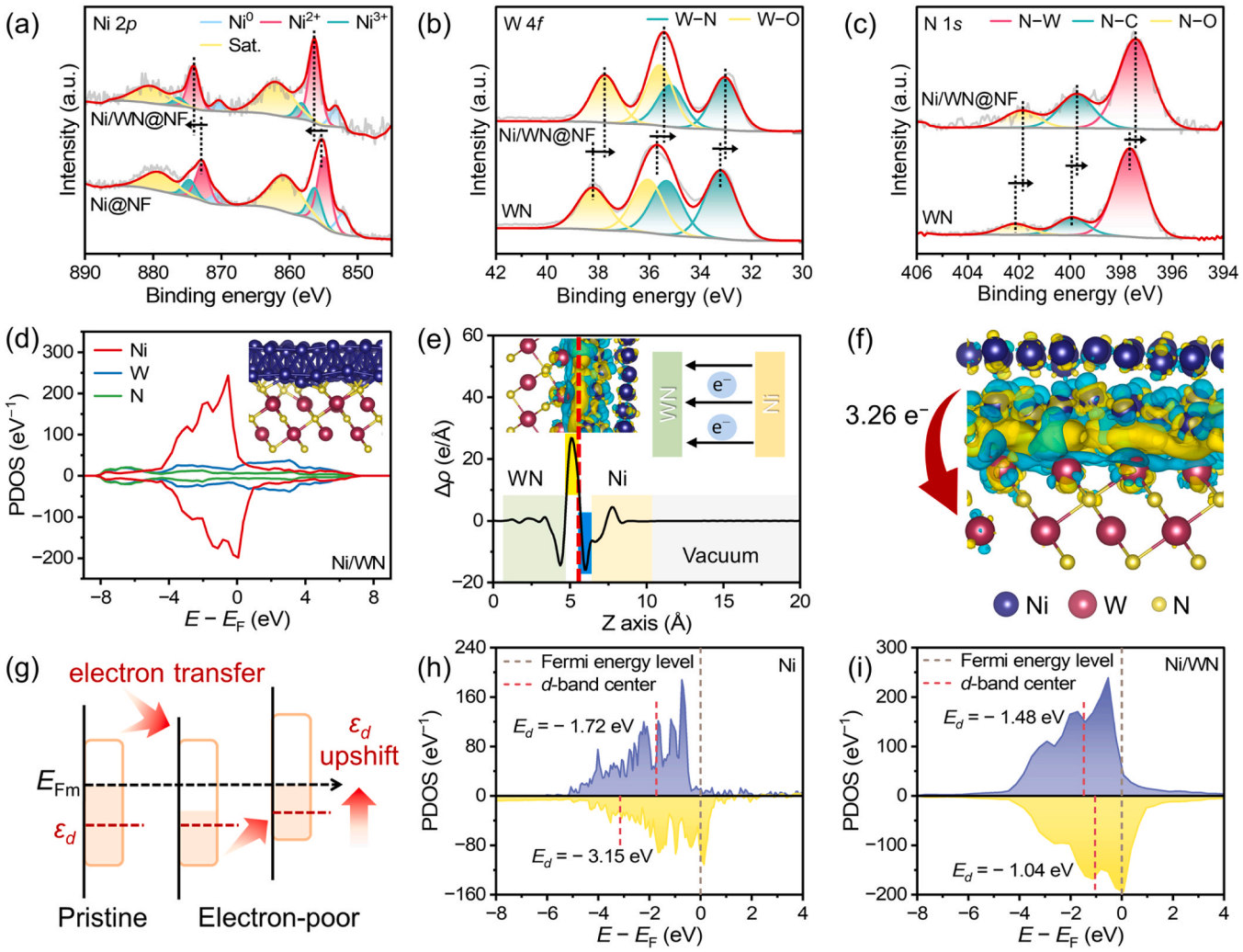

Fig. 3. Electronic structure of Ni/WN. (a) High-resolution XPS spectra of Ni 2 *p* of Ni/WN@NF and Ni@NF. High-resolution XPS spectra of (b) W 4 *f* and (c) N 1 *s* of Ni/WN@NF and WN. (d) Projected density of states of Ni/WN. (e, f) Charge density difference at the Ni/WN interface. The yellow and blue isosurfaces represent charge accumulation and depletion in space, respectively. (g) Schematic diagram of the enhancement of the *d*-band center caused by electron deficiency at the Ni site. The DFT-estimated PDOS of Ni atoms in the *d* orbitals of (h) Ni and (i) Ni/WN. The dashed lines indicate the calculated *d*-band centers for spin-up and spin-down, respectively.

and significantly lower than those of Ni@NF (231 mV) and WN@NF (183 mV). Moreover, Ni/WN@NF achieves 406 mA cm^{-2} at an overpotential of 200 mV, comparable to Pt/C@NF, indicating excellent HER activity. The HER kinetic behavior of the catalyst was further evaluated by the Tafel slope, as shown in Fig. 4b. The Tafel slope of Ni/WN@NF is 49 mV dec^{-1}, smaller than those of Ni@NF (84 mV dec^{-1}) and WN@NF (106 mV dec^{-1}), suggesting that the Ni/WN heterostructure follows the Volmer-Heyrovsky mechanism and exhibits more favorable HER reaction kinetics [45,46]. The Nyquist plots in Fig. 4c, fitted using the dual CPE model (Table S4), show that Ni/WN@NF (0.43 Ω cm^2) has a smaller charge transfer resistance (R_{ct}) compared to Ni@NF (12.33 Ω cm^2), indicating that electron transfer on the Ni surface is accelerated by forming a heterostructure with WN [47]. In addition, as shown in Fig. S32 and S33, Ni/WN@NF exhibits a large double-layer capacitance (C_{dl}) of 932.52 mF cm^{-2}, which is much higher than those of Pt/C@NF, Ni@NF, and WN@NF, suggesting that the integrated electrode structure facilitates the exposure of more active sites. Furthermore, Ni/WN@NF displays the highest C_{dl}-normalized HER activity, further demonstrating the enhanced intrinsic activity of the Ni/WN heterostructure.

To assess the alkaline HOR electrocatalysis, steady-state polarization curves for the Ni/WN@NF electrode were obtained in H_2- or Ar-saturated 0.1 M KOH (Fig. S34). The significantly enhanced anodic current density in H_2-saturated electrolytes demonstrates the excellent HOR electrocatalytic performance of the Ni/WN heterostructure. As shown in Fig. 4d, the current density of Ni/WN@NF at 50 mV reaches 4.13 mA cm^{-2}, which is higher than that of Pt/C@NF (3.77 mA cm^{-2}), Ni@NF (0.22 mA cm^{-2}), and WN@NF (0.16 mA cm^{-2}), implying that the synergistic effect on the interface can effectively enhance the HOR activity. Additionally, the exchange current densities (j_0) of these samples were extracted by linearly fitting the Butler-Volmer equation in the micropolarization region (Fig. 4e) [47,48]. Ni/WN@NF exhibits an exchange current density of 3.99 mA cm^{-2}, which is 5.5 and 14.3 times higher than that of Ni@NF and WN@NF, respectively, indicating the Ni/WN heterostructure's promising activity towards alkaline HOR.

The synthesis conditions, including the amount of nickel nitrate added during the hydrothermal process and the heat treatment duration in the ammonia atmosphere during annealing, were optimized. To investigate the effect of the Ni source on the catalytic activity, Ni/WN@NF-0, where only NF was used as the Ni source, was prepared. As shown in Fig. S35, the addition of nickel nitrate significantly enhances the N 1 *s* signal of XPS, and increases the content of Ni element from 1.27 % to 3.93 %. To determine the optimal nickel nitrate concentration, a series of Ni/WN heterostructure materials (Ni/WN@NF-50, Ni/WN@NF, and Ni/WN@NF-150) were synthesized at different

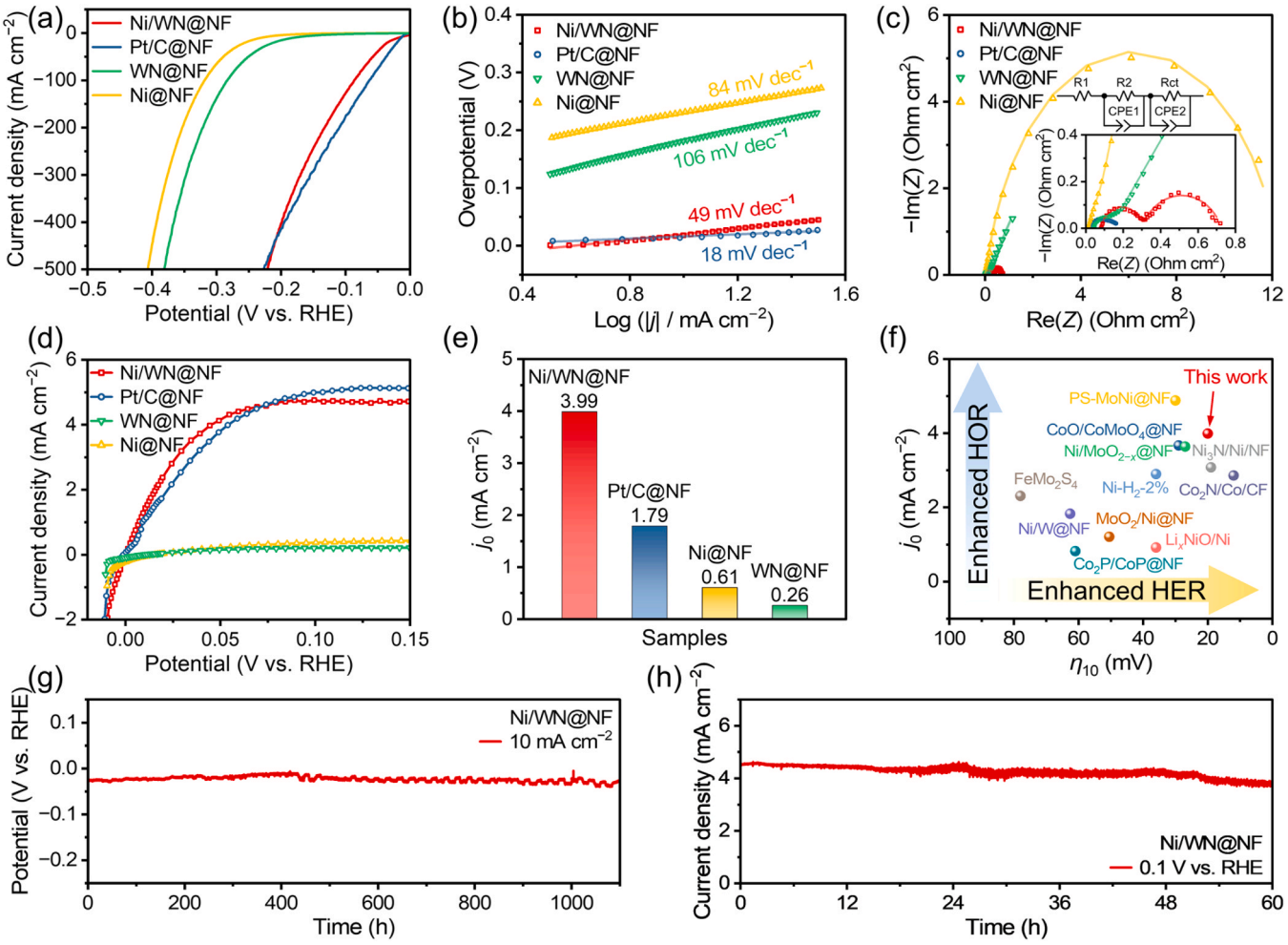

Fig. 4. HER/HOR performance of Ni/WN@NF. (a) HER polarization curves of Ni/WN@NF, Pt/C@NF, WN@NF, and Ni@NF. (b) The corresponding Tafel plots of these electrocatalysts. (c) EIS Nyquist plots of the catalysts obtained in the frequency range of 200,000–0.01 Hz, with the insets showing the magnified image and the fitted circuit model. (d) HOR steady-state polarization curves of Ni/WN@NF, Pt/C@NF, WN@NF, and Ni@NF. (e) The corresponding exchange current densities of these samples. (f) Comparison of HER and HOR activities of Ni/WN@NF with other recently reported electrocatalysts [10,12,15,16,47,49–54]. (g) Long-term HER stability of the Ni/WN@NF electrode measured at the current density of 10 mA cm^{-2} for 1100 h. (h) Long-term HOR stability of the Ni/WN@NF electrode measured at 0.1 V vs. RHE.

nickel nitrate concentrations of 50, 100, and 150 mmol/L (Fig. S36 and S37). When the nickel nitrate concentration is too high, agglomeration occurs on the surface of Ni/WN@NF-150 (Fig. S38). Subsequent electrochemical HER and HOR activity tests (Fig. S39 and S40) show that the catalyst exhibits the best HER/HOR activity when the nickel nitrate addition concentration is 100 mmol/L, making it the selected target concentration. Additionally, to explore the effect of WN content in the heterostructure on catalytic activity, retention times of 0, 1, 3, and 6 h in the ammonia atmosphere were tested (Ni/WN@NF-0h, Ni/WN@NF-1h, Ni/WN@NF, and Ni/WN@NF-6h). Ni/WN@NF-0h primarily retains the precursor structure, while the samples kept for 1, 3, and 6 h form Ni/WN heterostructures (Fig. S41 and S42). High-resolution XPS spectral analysis (Fig. S43 and S44) shows that the WN: Ni ratio in these samples increases with longer ammonia annealing time. HER and HOR polarization curves (Fig. S45 and S46) indicate that Ni/WN@NF exhibits the best H_2 electrocatalytic activity, as evidenced by the higher current density at a specified potential. Therefore, the heterostructure composed of appropriate amounts of WN and Ni can serve as an excellent alkaline HER/HOR electrocatalyst.

The outstanding catalytic activity of Ni/WN@NF is not only reflected in the HER, reaching 10 mA cm^{-2} at an overpotential of just 20 mV, but also in the HOR, with an exchange current density of 3.99 mA cm^{-2}, surpassing previously reported alkaline HER/HOR catalysts (Fig. 4f and Table S5) [10,12,15,16,47,49–54]. To further evaluate the HER/HOR catalytic performance of the Ni/WN@NF electrode, long-term operational stability was verified. Ni/WN@NF maintained excellent activity in a continuous HER stability test at a current density of 10 mA cm^{-2} for 1100 h (Fig. 4g), exhibiting an overpotential of only 25 mV. No observable changes in morphology, valence state, and structure were detected after the stability test, as confirmed by XRD, SEM, XPS, and TEM analyses (Fig. S47–S50). Additionally, Ni/WN@NF operated stably at a high current density of 100 mA cm^{-2} for over 90 h (Fig. S51–S54), demonstrating robust HER stability. As displayed in Fig. 4h, the electrochemical durability of HOR at an overpotential of 100 mV was measured by chronoamperometry. Remarkably, after 60 h of continuous testing, Ni/WN@NF retained 85 % of its initial current density. Meanwhile, the crystal structure and morphology remained intact after the durability test (Fig. S55–S58), indicating that the Ni/WN heterostructure possesses excellent HOR durability. Furthermore, to demonstrate that the synthesis strategy of the integrated Ni/WN catalyst can be extended to other substrates, Ni/WN@CP was experimentally prepared (Fig. S59 and S60), which also exhibited excellent HER/HOR catalytic activity.

To identify the catalytically active sites in the Ni/WN heterostructure, thiocyanate poisoning experiments were conducted. SCN^- can strongly coordinate with metal atoms, complexing with Ni nanoparticles

and inactivating them [55–57]. As shown in Fig. S61 and S62, the HER activity of Ni/WN@NF progressively decreased with the addition of KSCN. In the comparative tests, 5 mM of potassium thiocyanate was added to the electrolyte. As shown in Fig. 5a, the HER activity of Ni/WN@NF was significantly reduced, as evidenced by the overpotential increase from 20 mV to 102 mV at a current density of 10 mA cm^{-2}. In terms of HOR (Fig. 5b), the catalytic activity of Ni/WN@NF deteriorated substantially after the addition of KSCN, with the current density at an overpotential of 50 mV dropping from 4.13 mA cm^{-2} to only 0.38 mA cm^{-2}. The corresponding Tafel slopes (Fig. 5c and S63) and exchange current densities (Fig. 5d) indicate that the HER/HOR activities of Ni/WN and Ni decrease significantly, while WN shows less change, suggesting that the Ni site is the primary active site for HER/HOR electrocatalysis in the Ni/WN heterostructure. Therefore, it is concluded that the heterostructure-induced Ni can enhance the alkaline HER/HOR kinetics.

3.4. Mechanistic understanding of enhanced HER/HOR activity

Density functional theory was employed to further investigate the possible effects of forming heterostructures with WN on the HER/HOR activity of Ni. The HER mechanism in alkaline media involves three key processes: the Volmer step of water dissociation, *OH desorption, and *H conversion to H_2 [58]. The HOR process is essentially the reverse of the HER process [8], and the energy changes for each intermediate step were calculated [59]. The free energy diagram is presented in Fig. 5e, with the corresponding adsorption models shown in Fig. S3 and S64–S71. Initially, the adsorption energies of *H on Ni, WN, and Ni/WN were determined to be −0.474, 0.039, and −0.507 eV, respectively, indicating that Ni/WN is the most favorable catalyst for *H adsorption. Furthermore, the free energy of *H + *OH adsorbed on Ni was 0.157 eV, while the adsorption of *H + *OH on Ni/WN exhibited a negative free energy (−0.120 eV), suggesting that this reaction step is thermodynamically favorable for Ni/WN. The energy required for the combination of *H and *OH to form *H_2O on Ni, WN, and Ni/WN was calculated to be 0.350, 1.400, and 0.621 eV, respectively. It seems that the formation of water is more likely to occur on the Ni catalyst. However, the energy barrier in this process is crucial and cannot be ignored, which will be analyzed afterwards. Lastly, the free energy of *H_2O release on Ni, WN, and Ni/WN was determined to be −0.033, −0.508, and 0.006 eV, respectively. To better understand the role of heterostructure-induced Ni in alkaline H_2 electrocatalysis, it is essential to examine the Volmer step transition states (TS) between Ni/WN heterostructure and Ni.

The Volmer step in the HER/HOR process involves the interconversion between adsorbed *H_2O and *H + *OH. Here, *H, *OH, and *H_2O

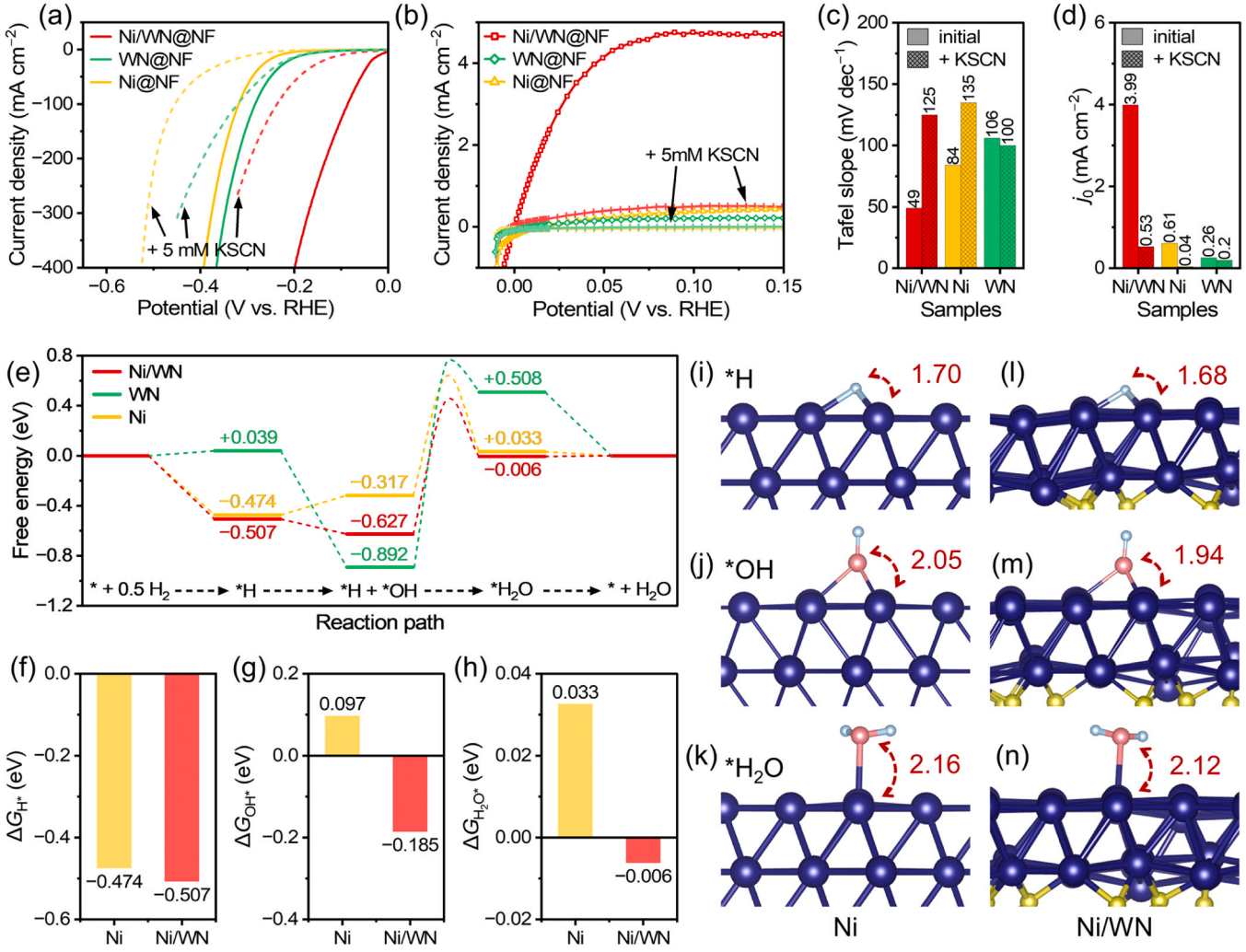

Fig. 5. Source of H_2 electrocatalytic activity of Ni/WN. (a) HER and (b) HOR polarization curves of Ni/WN@NF, WN@NF, and Ni@NF before and after adding KSCN. (c) Tafel slopes of HER and (d) exchange current densities of HOR for these samples before and after adding KSCN. (e) Calculated adsorption free energy diagram of alkaline HOR on Ni/WN, WN, and Ni. Calculated adsorption free energies of (f) *H, (g) *OH, and (h) *H_2O on Ni and Ni/WN. Optimized structures of (i) *H, (j) *OH, and (k) *H_2O adsorbed on Ni. Optimized structures of (l) *H, (m) *OH, and (n) *H_2O adsorbed on Ni/WN. The unit of the data representing distances in (i–n) is Å.

are all critical adsorption intermediates involved in the HER/HOR process. The formation of a heterostructure with WN induces electron depletion in Ni, which raises its *d*-band center and enhances its surface adsorption capability. DFT calculations confirm that the Ni/WN heterostructure exhibits stronger adsorption of *H, *OH, and *H_2O compared to metallic Ni (Fig. 5f–h, S4, and S72). Additionally, the calculated distances between these intermediates and the Ni site are shorter in the heterostructure. As shown in Fig. 5i–n, the distances from *H, *OH, and *H_2O to the Ni site in Ni/WN are 1.68, 1.94, and 2.12 Å, respectively, which are shortened by 0.02, 0.11, and 0.04 Å relative to pure Ni, further confirming the enhanced adsorption strength toward key intermediates.

Analyzing the adsorption of intermediates on the catalyst surface provides insights into the transition states, making *in-situ* Raman spectroscopy an essential tool for studying the Helmholtz layer (Fig. 6a). The Ni/WN@NF and Ni@NF catalysts were analyzed, with a specific focus on interfacial water, as *H_2O is the reactant in the Volmer step during HER. The Raman band of interfacial water (3000–3800 cm^{-1}) was deconvoluted using Gaussian fitting (Fig. 6b and S73–S74) and categorized into three distinct O–H stretching modes (Fig. 6c): 4-coordinate hydrogen-bonded water (4-HB·H_2O, green), 2-coordinate hydrogen-bonded water (2-HB·H_2O, yellow), and weakly hydrogen-bonded K-ion hydrated water (K^+·H_2O, blue) [18,19]. The relative proportions of these interfacial water modes were analyzed (Fig. S75 and S76). Under increasingly negative potentials, the content of 4-HB·H_2O on Ni/WN@NF decreased, while 2-HB·H_2O and K^+·H_2O increased, reflecting the disruption of the hydrogen-bond network during the alkaline HER [18]. The relative content of 4-HB·H_2O was used to quantify this destruction. As shown in Fig. 6d, the content of 4-HB·H_2O on Ni/WN@NF remains consistently lower than that on Ni@NF across various potentials. Furthermore, the 4-HB·H_2O content decreases progressively during the HER process (Fig. 6e), indicating a stronger

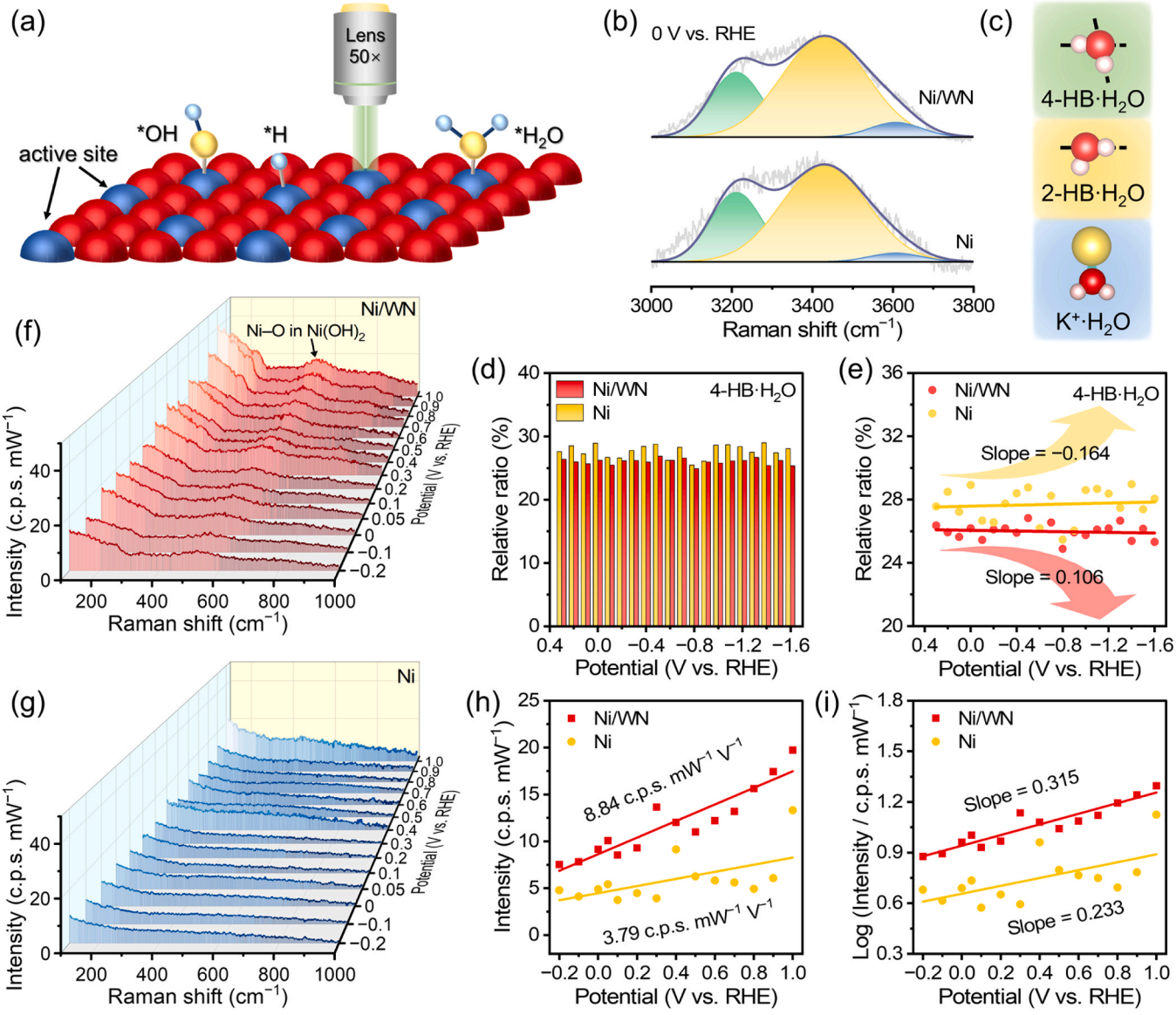

Fig. 6. *In-situ* Raman spectroscopy verification. (a) Schematic diagram of *in-situ* Raman spectroscopy measurements. (b) Raman spectra of interfacial water on Ni/WN@NF and Ni@NF electrodes at 0 V vs. RHE in 1 M KOH solution fitted by Gaussian. (c) Schematic diagram of the three O–H stretching modes. (d, e) Relative proportion of 4-coordinate hydrogen-bonded water (4-HB·H_2O) in interfacial water of Ni/WN@NF and Ni@NF at different potentials. *In-situ* Raman spectra of (f) Ni/WN@NF and (g) Ni@NF in 1 M KOH at different potentials. (h) Statistics of the maximum intensity of Ni–O and Ni–OH vibration bands of Ni/WN@NF and Ni@NF at different potentials. (i) Logarithm of the maximum intensity of Ni–O and Ni–OH vibration bands of Ni/WN@NF and Ni@NF at different potentials. c.p.s., counts per second.

disruption of the hydrogen-bond network in the inner Helmholtz layer. This disruption demonstrates the enhanced interaction between the heterostructure-induced Ni and water molecules, which weakens the H–O–H bonds of adsorbed water, thereby promoting *H_2O dissociation [60,61].

In the Volmer step of alkaline HOR, *H and *OH are crucial intermediates, but Ni typically exhibits poor *OH adsorption. Enhancing *OH adsorption on Ni sites is the key to improving HOR activity [26]. *In-situ* Raman spectroscopy was employed to study *OH adsorption on the samples in the Helmholtz layer (Fig. 6f and 6g). As the applied potential increased from −0.2 to 1.0 V, the intensities of the Ni–O and Ni–OH vibration bands (450–560 cm^{-1}) gradually increased [62]. As shown in Fig. 6h, the maximum intensity of the vibration bands increase with increasing potential. To account for differences in initial signal intensity between Ni/WN and Ni, logarithmic analysis was applied (Fig. 6i). The slope of the logarithmic intensity versus potential for Ni/WN@NF is significantly higher, indicating that the Ni–O and Ni–OH vibrations exhibit greater sensitivity to the applied potential in the heterostructure. This enhanced sensitivity arises from the electron transfer from Ni to WN within the Ni/WN heterostructure, which creates a positive charge center at the Ni site. This facilitates electron transfer from OH^- to WN through a built-in electric field, improving electron transport and interaction with OH^- at the Helmholtz layer.

Fig. 7a summarizes the experimental and computational findings for Ni/WN and Ni. Experimentally, *in-situ* Raman spectroscopy demonstrates that the Ni/WN heterostructure exerts a stronger influence on *H_2O and *OH than Ni, evidenced by a lower relative proportion of 4-HB·H_2O and greater sensitivity to Ni–O and Ni–OH vibrations. The Ni/WN heterostructure also exhibits superior HER and HOR activities, as reflected by a lower Tafel slope and higher exchange current density. Computationally, the optimized structure reveals that *H, *OH, and *H_2O are closer to the Ni/WN surface than Ni alone. Based on these, further discussions are provided below to elucidate the structure–activity relationship of Ni/WN.

Enhanced adsorption of *H, *OH, and *H_2O facilitates the formation and dissociation of *H_2O, accelerating the slow Volmer step of alkaline HER/HOR [63]. Fig. 7b–d illustrate these mechanisms. During *H_2O formation, the Ni/WN heterostructure enhances *H and *OH adsorption, bringing them closer to the Ni active sites. The distance between *H and *OH adsorbed on adjacent Ni sites decreases from 3.01 Å to 2.82 Å,

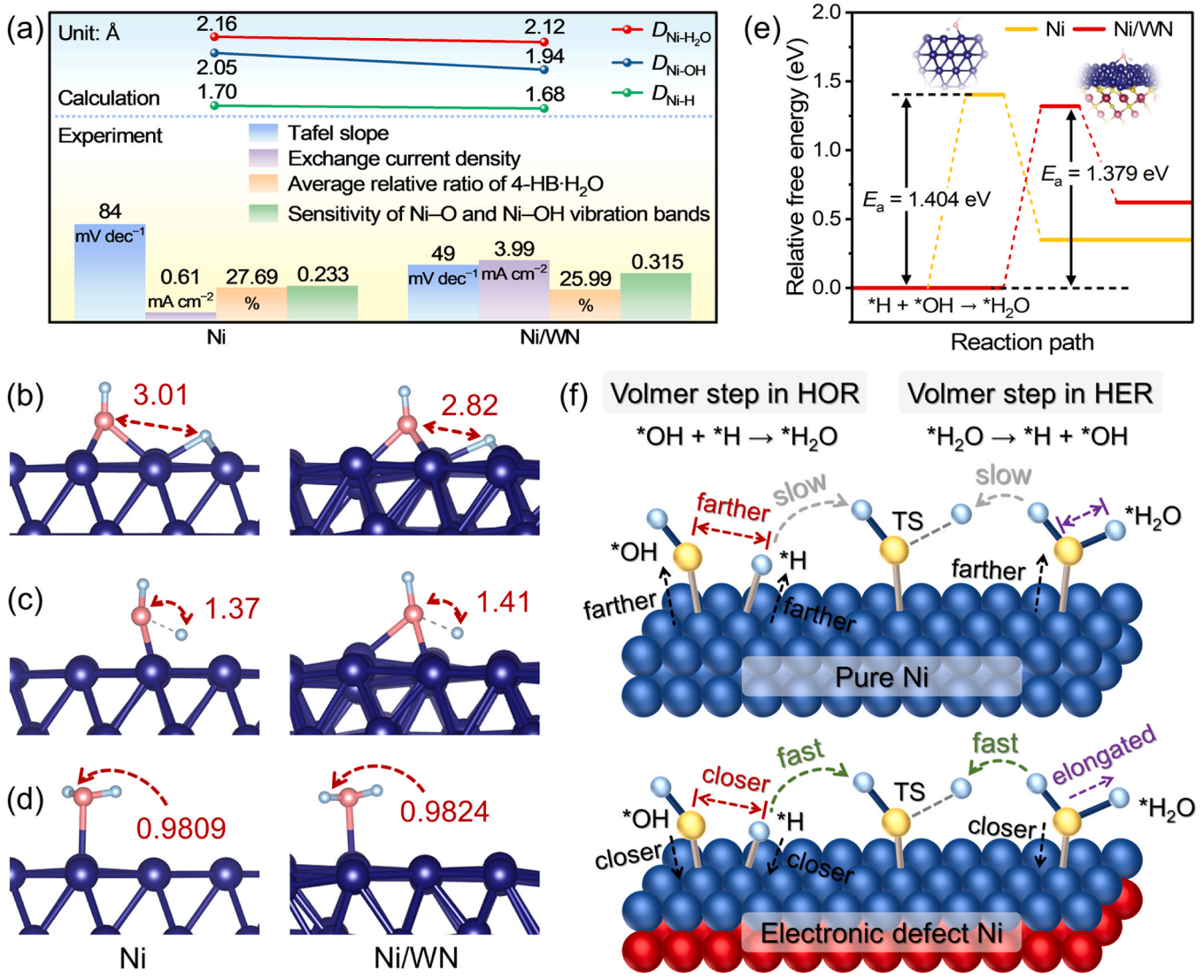

Fig. 7. Mechanistic understanding of enhanced HER/HOR activity. (a) Effect of intermediates' adsorption on the performance of alkaline HER/HOR. (b) Optimized structures of *H and *OH adsorbed on Ni and Ni/WN. (c) Optimized structures of the Volmer step transition states (TS) of Ni and Ni/WN. (d) Optimized structures of water molecules adsorbed on Ni and Ni/WN. (e) Volmer step reaction barriers for adsorbed *H and *OH to form *H_2O on Ni and Ni/WN. (f) Schematic diagram of the heterostructure-induced Ni HER/HOR kinetic enhancement mechanism. The unit of the data representing distances in (b–d) is Å.

reducing the energy barrier for the *H + *OH → TS transition. For *H_2O dissociation, the H–OH bond length of adsorbed *H_2O increases from 0.9809 Å (Ni) to 0.9824 Å (Ni/WN), suggesting that water adsorbed on Ni/WN is more likely to dissociate [64]. Transition state calculations for the Volmer step (Fig. 7e and S77–S78) reveal that the energy barrier on Ni (1.404 eV) is the rate-determining step of alkaline HOR. In contrast, Ni/WN reduces this barrier to 1.379 eV, making the reaction more kinetically favorable [27]. In terms of alkaline HER, the Volmer step is still the rate-determining step, and Ni/WN heterostructure also exhibits a lower energy barrier. Thus, the proposed mechanistic pathway is illustrated schematically in Fig. 7f to highlight the role of heterostructure-induced modulation. The heterostructure-induced Ni enhances *H, *OH, and *H_2O adsorption, shortens the *H–*OH distance, elongates the H–OH bond of *H_2O, and lowers the transition state energy barrier, thereby significantly optimizing the Helmholtz layer and improving alkaline HER/HOR kinetics.

4. Conclusions

In conclusion, Ni/WN heterostructures were successfully designed and synthesized on nickel foam through a straightforward two-step approach. XAS, XPS, and differential charge density analysis revealed electron transfer from Ni to WN, leading to localized electron depletion around the Ni site. This electron loss at the Ni site shifted the *d*-band center of Ni upward, thereby enhancing the adsorption of *OH and *H_2O on the Ni/WN surface and improving the alkaline HER/HOR kinetics. Consequently, Ni/WN@NF demonstrated outstanding activity, requiring an overpotential of only 20 mV to drive a current density of 10 mA cm^{-2} for HER and achieving an exchange current density of 3.99 mA cm^{-2} for HOR. *In-situ* Raman spectroscopy and DFT calculations jointly confirmed that the Ni/WN heterostructure exhibited stronger *OH and *H_2O adsorption than Ni in the inner Helmholtz layer, brought *H and *OH closer, prolonged the H–OH bonds of the adsorbed water molecules, and reduced the energy barrier for *H_2O formation/dissociation. Overall, this study is of great significance, not only enriching the understanding of the catalytic kinetics of Ni-based materials in alkaline HER/HOR but also offering a versatile approach that can be extended to the design of other heterostructured materials with high performance for catalytic applications.

CRediT authorship contribution statement

Wanli Liang: Writing – review & editing, Writing – original draft, Methodology, Investigation, Data curation, Conceptualization. **Zixuan Dan:** Investigation, Data curation. **Xiyu Gong:** Investigation, Data curation. **Jinchang Xu:** Methodology, Investigation. **Hongjuan Wang:** Writing – review & editing, Supervision. **Yonghai Cao:** Writing – review & editing, Supervision. **Hao Yu:** Writing – review & editing, Supervision. **Yanshuo Jin:** Writing – review & editing, Supervision, Funding acquisition, Conceptualization. **Hao-Fan Wang:** Writing – review & editing, Supervision, Funding acquisition, Conceptualization.

Declaration of Competing Interest

The authors declare that they have no known competing financial interests or personal relationships that could have appeared to influence the work reported in this paper.

Acknowledgements

This work is financially supported by National Natural Science Foundation of China (No. 22209049, 22005120), Natural Science Foundation of Guangdong Province (No. 2023A1515012804, 2025A1515010003), and Science and Technology Program of Guangzhou (No. 2023A04J0674). The authors sincerely acknowledge Senior Researcher Zhenyou Wang and his group at the Greater Bay Area Aerospace Information Research Institute for their kind assistance with Raman spectroscopy measurements.

Appendix A. Supporting information

Supplementary data associated with this article can be found in the online version at doi:10.1016/j.apcatb.2025.126069.

Data availability

Data will be made available on request.

References

[1] I.H. Kwak, J.Y. Kim, G.M. Zewdie, J. Yang, K. Lee, S.J. Yoo, I.S. Kwon, J. Park, H. S. Kang, Electrocatalytic activation in $ReSe_2$-VSe_2 alloy nanosheets to boost Water-Splitting hydrogen evolution reaction, Adv. Mater. (2024) 2310769, https://doi.org/10.1002/adma.202310769.
[2] X. Zou, Y. Zhang, Noble metal-free hydrogen evolution catalysts for water splitting, Chem. Soc. Rev. 44 (2015) 5148–5180, https://doi.org/10.1039/C4CS00448E.
[3] H.A. Gasteiger, N.M. Marković, Just a Dream—or future reality? Science 324 (2009) 48–49, https://doi.org/10.1126/science.1172083.
[4] W. Sheng, A.P. Bivens, M. Myint, Z. Zhuang, R.V. Forest, Q. Fang, J.G. Chen, Y. Yan, Non-precious metal electrocatalysts with high activity for hydrogen oxidation reaction in alkaline electrolytes, Energy Environ. Sci. 7 (2014) 1719–1724, https://doi.org/10.1039/C3EE43899F.
[5] Z. Zhuang, S.A. Giles, J. Zheng, G.R. Jenness, S. Caratzoulas, D.G. Vlachos, Y. Yan, Nickel supported on nitrogen-doped carbon nanotubes as hydrogen oxidation reaction catalyst in alkaline electrolyte, Nat. Commun. 7 (2016) 10141, https://doi.org/10.1038/ncomms10141.
[6] L. Gao, Y. Wang, H. Li, Q. Li, N. Ta, L. Zhuang, Q. Fu, X. Bao, A nickel nanocatalyst within a h-BN shell for enhanced hydrogen oxidation reactions, Chem. Sci. 8 (2017) 5728–5734, https://doi.org/10.1039/c7sc01615h.
[7] J.K. Nørskov, T. Bligaard, A. Logadottir, J.R. Kitchin, J.G. Chen, S. Pandelov, U. Stimming, Trends in the exchange current for hydrogen evolution, J. Electrochem. Soc. 152 (2005) J23–J26, https://doi.org/10.1149/1.1856988.
[8] I.T. McCrum, M.T.M. Koper, The role of adsorbed hydroxide in hydrogen evolution reaction kinetics on modified platinum, Nat. Energy 5 (2020) 891–899, https://doi.org/10.1038/s41560-020-00710-8.
[9] Y. Yang, X. Sun, G. Han, X. Liu, X. Zhang, Y. Sun, M. Zhang, Z. Cao, Y. Sun, Enhanced electrocatalytic hydrogen oxidation on Ni/NiO/C derived from a Nickel-Based Metal–Organic framework, Angew. Chem. 131 (2019) 10754–10759, https://doi.org/10.1002/ange.201905430.
[10] W. Liang, M. Zhou, X. Li, L. Zhu, Z. Li, Y. Zhou, J. Chen, F. Xie, H.-F. Wang, N. Wang, Y. Jin, H. Meng, Oxygen-vacancy-rich MoO_2 supported nickel as electrocatalysts to promote alkaline hydrogen evolution and oxidation reactions, Chem. Eng. J. 464 (2023) 142671, https://doi.org/10.1016/j.cej.2023.142671.
[11] Y. Duan, X. Zhang, F. Gao, Y. Kong, Y. Duan, X. Yang, X. Yu, Y. Wang, S. Qin, Z. Chen, R. Wu, P. Yang, X. Zheng, J. Zhu, M. Gao, T. Lu, Z. Yu, S. Yu, Interfacial engineering of Ni/V_2O_3 heterostructure catalyst for boosting hydrogen oxidation reaction in alkaline electrolytes, Angew. Chem. Int. Ed. 62 (2023) e202217275, https://doi.org/10.1002/anie.202217275.
[12] F. Song, W. Li, J. Yang, G. Han, P. Liao, Y. Sun, Interfacing nickel nitride and nickel boosts both electrocatalytic hydrogen evolution and oxidation reactions, Nat. Commun. 9 (2018) 4531, https://doi.org/10.1038/s41467-018-06728-7.
[13] X. Chen, B. Sun, Q. Song, Z. Wang, C. Qin, M.A. Majeed, C. Chen, D. Sun, K. Zhang, M. Zhao, Tuning the hydrogen bond network inside the helmholtz plane for industrial hydrogen evolution, Adv. Funct. Mater. (2025) 2503701, https://doi.org/10.1002/adfm.202503701.
[14] B. Zhang, L. Zhang, Q. Tan, J. Wang, J. Liu, H. Wan, L. Miao, J. Jiang, Simultaneous interfacial chemistry and inner helmholtz plane regulation for superior alkaline hydrogen evolution, Energy Environ. Sci. 13 (2020) 3007–3013, https://doi.org/10.1039/D0EE02020F.
[15] J. Song, Y.Q. Jin, L. Zhang, P. Dong, J. Li, F. Xie, H. Zhang, J. Chen, Y. Jin, H. Meng, X. Sun, Phase-Separated Mo–Ni alloy for hydrogen oxidation and evolution reactions with high activity and enhanced stability, Adv. Energy Mater. 11 (2021) 2003511, https://doi.org/10.1002/aenm.202003511.
[16] W. Liang, Z. Le, P. Dong, Z. Dan, J. Chen, H. Zhang, J. Chen, F. Xie, N. Wang, Y. Jin, H. Meng, Janus bimetallic materials as efficient electrocatalysts for hydrogen oxidation and evolution reactions, J. Colloid Interface Sci. 625 (2022) 128–135, https://doi.org/10.1016/j.jcis.2022.06.029.
[17] R. Ram, L. Xia, H. Benzidi, A. Guha, V. Golovanova, A. Garzón Manjón, D. Llorens Rauret, P. Sanz Berman, M. Dimitropoulos, B. Mundet, E. Pastor, V. Celorrio, C. A. Mesa, A.M. Das, A. Pinilla-Sánchez, S. Giménez, J. Arbiol, N. López, F.P. García de Arquer, Water-hydroxide trapping in cobalt tungstate for proton exchange membrane water electrolysis, Science 384 (2024) 1373–1380, https://doi.org/10.1126/science.adk9849.
[18] S. Wang, T. Jiang, Y. Hao, J. Wu, C. Lei, Z. Chen, W. Du, M. Gong, Unveiling the cation dependence in alkaline hydrogen evolution by differently-charged ruthenium/molybdenum sulfide hybrids, Adv. Mater. 36 (2024) 2410422, https://doi.org/10.1002/adma.202410422.

[19] Y.-H. Wang, S. Zheng, W.-M. Yang, R.-Y. Zhou, Q.-F. He, P. Radjenovic, J.-C. Dong, S. Li, J. Zheng, Z.-L. Yang, G. Attard, F. Pan, Z.-Q. Tian, J.-F. Li, *in situ* Raman spectroscopy reveals the structure and dissociation of interfacial water, Nature 600 (2021) 81–85, https://doi.org/10.1038/s41586-021-04068-z.

[20] G. Kresse, J. Furthmüller, Efficient iterative schemes for ab initio total-energy calculations using a plane-wave basis set, Phys. Rev. B 54 (1996) 11169–11186, https://doi.org/10.1103/PhysRevB.54.11169.

[21] G. Kresse, D. Joubert, From ultrasoft pseudopotentials to the projector augmented-wave method, Phys. Rev. B 59 (1999) 1758–1775, https://doi.org/10.1103/PhysRevB.59.1758.

[22] J.P. Perdew, K. Burke, M. Ernzerhof, Generalized gradient approximation made simple, Phys. Rev. Lett. 77 (1996) 3865–3868, https://doi.org/10.1103/PhysRevLett.77.3865.

[23] S. Grimme, J. Antony, S. Ehrlich, H. Krieg, A consistent and accurate ab initio parametrization of density functional dispersion correction (DFT-D) for the 94 elements H-Pu, J. Chem. Phys. 132 (2010) 154104, https://doi.org/10.1063/1.3382344.

[24] B. Hammer, J.K. Nørskov, Electronic factors determining the reactivity of metal surfaces, Surf. Sci. 343 (1995) 211–220, https://doi.org/10.1016/0039-6028(96)80007-0.

[25] Q. Li, X. Zou, X. Ai, H. Chen, L. Sun, X. Zou, Revealing activity trends of metal diborides toward pH-Universal hydrogen evolution electrocatalysts with Pt-Like activity, Adv. Energy Mater. 9 (2019) 1803369, https://doi.org/10.1002/aenm.201803369.

[26] Y. Men, X. Su, P. Li, Y. Tan, C. Ge, S. Jia, L. Li, J. Wang, G. Cheng, L. Zhuang, S. Chen, W. Luo, Oxygen-Inserted Top-Surface layers of ni for boosting alkaline hydrogen oxidation electrocatalysis, J. Am. Chem. Soc. 144 (2022) 12661–12672, https://doi.org/10.1021/jacs.2c01448.

[27] T. Tang, X. Liu, X. Luo, Z. Xue, H. Pan, J. Fu, Z. Yao, Z. Jiang, Z. Lyu, L. Zheng, D. Su, J.-N. Zhang, L. Zhang, J. Hu, Unconventional bilateral compressive strained Ni–Ir interface synergistically accelerates alkaline hydrogen oxidation, J. Am. Chem. Soc. 145 (2023) 13805–13815, https://doi.org/10.1021/jacs.3c02487.

[28] W. Liang, M. Zhou, X. Lin, J. Xu, P. Dong, Z. Le, M. Yang, J. Chen, F. Xie, N. Wang, Y. Jin, H. Meng, Nickel-doped tungsten oxide promotes stable and efficient hydrogen evolution in seawater, Appl. Catal. B Environ. 325 (2023) 122397, https://doi.org/10.1016/j.apcatb.2023.122397.

[29] Z. Dan, W. Liang, X. Gong, X. Lin, W. Zhang, Z. Le, F. Xie, J. Chen, M. Yang, N. Wang, Y. Jin, H. Meng, Substitutional doping engineering toward W_2N nanorod for hydrogen evolution reaction at high current density, ACS Mater. Lett. 4 (2022) 1374–1380, https://doi.org/10.1021/acsmaterialslett.2c00324.

[30] S. Tan, Y. Dai, Y. Jiang, Q. Wei, G. Zhang, F. Xiong, X. Zhu, Z. Hu, L. Zhou, Y. Jin, K. Kanamura, Q. An, L. Mai, Revealing the origin of highly efficient polysulfide anchoring and transformation on Anion-Substituted vanadium nitride host, Adv. Funct. Mater. 31 (2021) 2008034, https://doi.org/10.1002/adfm.202008034.

[31] S. Ouendi, K. Robert, D. Stievenard, T. Brousse, P. Roussel, C. Lethien, Sputtered tungsten nitride films as pseudocapacitive electrode for on chip micro-supercapacitors, Energy Storage Mater. 20 (2019) 243–252, https://doi.org/10.1016/j.ensm.2019.04.006.

[32] F. Gao, Q. Wan, J. Yuan, R. Lei, S. Lin, P. Liu, Highly efficient and durable core-shell catalyst with dual functions: tungsten nitride quantum dots encapsulated in ultra-thin graphene, Appl. Catal. B Environ. 299 (2021) 120692, https://doi.org/10.1016/j.apcatb.2021.120692.

[33] F. Liu, L. Li, F. Mo, J. Chen, S. Deng, N. Xu, A Catalyzed-Growth route to directly form micropatterned WO_2 and WO_3 nanowire arrays with excellent field emission behaviors at low temperature, Cryst. Growth Des. 10 (2010) 5193–5199, https://doi.org/10.1021/cg100995f.

[34] Z. Kou, T. Wang, H. Wu, L. Zheng, S. Mu, Z. Pan, Z. Lyu, W. Zang, S.J. Pennycook, J. Wang, Twinned tungsten carbonitride nanocrystals boost hydrogen evolution activity and stability, Small 15 (2019) 1900248, https://doi.org/10.1002/smll.201900248.

[35] N. Kaur, D. Zappa, V. Maraloiu, E. Comini, Novel Christmas branched like NiO/$NiWO_4$/WO_3 (p–p–n) nanowire heterostructures for chemical sensing, Adv. Funct. Mater. 31 (2021) 2104416, https://doi.org/10.1002/adfm.202104416.

[36] J. Li, D. Chu, D.R. Baker, R. Jiang, Seamless separation of OH_{ad} and H_{ad} on a Ni–O catalyst toward exceptional alkaline hydrogen evolution, J. Mater. Chem. A 10 (2022) 1278–1283, https://doi.org/10.1039/D1TA07303F.

[37] J. Jiao, W. Yang, Y. Pan, C. Zhang, S. Liu, C. Chen, D. Wang, Interface engineering of partially phosphidated Co@Co–P@NPCNTs for highly enhanced electrochemical overall water splitting, Small 16 (2020) 2002124, https://doi.org/10.1002/smll.202002124.

[38] C. Li, Y. Liu, Z. Zhuo, H. Ju, D. Li, Y. Guo, X. Wu, H. Li, T. Zhai, Local charge distribution engineered by schottky heterojunctions toward urea electrolysis, Adv. Energy Mater. 8 (2018) 1801775, https://doi.org/10.1002/aenm.201801775.

[39] T.-F. Li, J. Li, L.-P. Zhang, J.-W. Ke, M.-X. Fan, L.-F. Zhang, C.-W. Deng, Y. Sun, T. Qian, C.-L. Yan, Work-function-induced interfacial electron redistribution of MoO_2/WO_2 heterostructures for high-efficiency electrocatalytic hydrogen evolution reaction, Rare Met 43 (2024) 489–499, https://doi.org/10.1007/s12598-023-02516-5.

[40] H. Yu, X. Yang, X. Xiao, M. Chen, Q. Zhang, L. Huang, J. Wu, T. Li, S. Chen, L. Song, L. Gu, B.Y. Xia, G. Feng, J. Li, J. Zhou, Atmospheric-pressure synthesis of 2D nitrogen-rich tungsten nitride, Adv. Mater. 30 (2018) 1805655, https://doi.org/10.1002/adma.201805655.

[41] M. Ning, Y. Wang, L. Wu, L. Yang, Z. Chen, S. Song, Y. Yao, J. Bao, S. Chen, Z. Ren, Hierarchical interconnected NiMoN with large specific surface area and high mechanical strength for efficient and stable alkaline Water/Seawater hydrogen evolution, NanoMicro Lett. 15 (2023) 157, https://doi.org/10.1007/s40820-023-01129-y.

[42] L. Meng, S. Shang, S. Liu, L. Zhang, Q. Tang, H. Wang, F. Wang, C. Li, Y. Sun, H. Wu, Cooperative effects between NiMo alloy enable highly efficient for all-pH-value and alkaline seawater hydrogen evolution, Appl. Catal. B Environ. Energy 358 (2024) 124388, https://doi.org/10.1016/j.apcatb.2024.124388.

[43] D. Zha, R. Wang, S. Tian, Z.-J. Jiang, Z. Xu, C. Qin, X. Tian, Z. Jiang, Defect engineering and carbon supporting to achieve Ni-Doped CoP_3 with high catalytic activities for overall water splitting, NanoMicro Lett. 16 (2024) 250, https://doi.org/10.1007/s40820-024-01471-9.

[44] Y. Wu, X. Liu, D. Han, X. Song, L. Shi, Y. Song, S. Niu, Y. Xie, J. Cai, S. Wu, J. Kang, J. Zhou, Z. Chen, X. Zheng, X. Xiao, G. Wang, Electron density modulation of $NiCo_2S_4$ nanowires by nitrogen incorporation for highly efficient hydrogen evolution catalysis, Nat. Commun. 9 (2018) 1425, https://doi.org/10.1038/s41467-018-03858-w.

[45] T. Zhang, L. Hang, Q. Liu, S. Tao, H. Bao, H.J. Fan, Positively charged hollow co nanoshells by kirkendall effect stabilized by electron sink for alkaline water dissociation, Adv. Mater. (2024) 2405386, https://doi.org/10.1002/adma.202405386.

[46] P. Han, N. Yao, W. Zuo, W. Luo, Manipulating the electronic structure of ni electrocatalyst through *d-p* orbital hybridization induced by B-*d*oping for efficient alkaline hydrogen oxidation reaction, Chin. J. Catal. 43 (2022) 1527–1534, https://doi.org/10.1016/S1872-2067(21)63955-4.

[47] G. Huang, W. Liang, Y. Wu, J. Li, Y.Q. Jin, H. Zeng, H. Zhang, F. Xie, J. Chen, N. Wang, Y. Jin, H. Meng, Co_2P/CoP hybrid as a reversible electrocatalyst for hydrogen oxidation/evolution reactions in alkaline medium, J. Catal. 390 (2020) 23–29, https://doi.org/10.1016/j.jcat.2020.07.023.

[48] S. Liu, Y. Wang, T. Jiang, S. Jin, M. Sajid, Z. Zhang, J. Xu, Y. Fan, X. Wang, J. Chen, Z. Liu, X. Zheng, K. Zhang, Q. Nian, Z. Zhu, Q. Peng, T. Ahmad, K. Li, W. Chen, Non-noble metal high-entropy alloy-based catalytic electrode for long-life hydrogen gas batteries, ACS Nano 18 (2024) 4229–4240, https://doi.org/10.1021/acsnano.3c09482.

[49] Z. Chen, Z. Guo, L. Zhu, Y. Che, M. Yang, Y. Zhou, J. Chen, F. Xie, N. Wang, Y. Jin, H. Meng, Interfacial coupling effect of CoO/$CoMoO_4$ promotes alkaline hydrogen electrode for hydrogen energy storage system, Int. J. Hydrog. Energy 48 (2023) 15809–15816, https://doi.org/10.1016/j.ijhydene.2023.01.097.

[50] W. Liang, P. Dong, Z. Le, X. Lin, X. Gong, F. Xie, H. Zhang, J. Chen, N. Wang, Y. Jin, H. Meng, Electron density modulation of MoO_2/Ni to produce superior hydrogen evolution and oxidation activities, ACS Appl. Mater. Interfaces 13 (2021) 39470–39479, https://doi.org/10.1021/acsami.1c11025.

[51] W. Ni, T. Wang, P.A. Schouwink, Y. Chuang, H.M. Chen, X. Hu, Efficient hydrogen oxidation catalyzed by Strain-Engineered nickel nanoparticles, Angew. Chem. Int. Ed. 59 (2020) 10797–10801, https://doi.org/10.1002/anie.201916314.

[52] F. Song, W. Li, J. Yang, G. Han, T. Yan, X. Liu, Y. Rao, P. Liao, Z. Cao, Y. Sun, Interfacial sites between cobalt nitride and cobalt act as bifunctional catalysts for hydrogen electrochemistry, ACS Energy Lett. 4 (2019) 1594–1601, https://doi.org/10.1021/acsenergylett.9b00738.

[53] K. Lu, Y. Liu, F. Lin, I.A. Cordova, S. Gao, B. Li, B. Peng, H. Xu, J. Kaelin, D. Coliz, C. Wang, Y. Shao, Y. Cheng, Li_xNiO/Ni heterostructure with strong basic lattice oxygen enables electrocatalytic hydrogen evolution with Pt-like activity, J. Am. Chem. Soc. 142 (2020) 12613–12619, https://doi.org/10.1021/jacs.0c00241.

[54] Z.-Y. Tian, X.-Q. Han, J. Du, Z.-B. Li, Y.-Y. Ma, Z.-G. Han, Bio-Inspired $FeMo_2S_4$ microspheres as bifunctional electrocatalysts for boosting hydrogen Oxidation/Evolution reactions in alkaline solution, ACS Appl. Mater. Interfaces 15 (2023) 11853–11865, https://doi.org/10.1021/acsami.2c22931.

[55] J. Ji, Y. Hou, S. Zhou, T. Qiu, L. Zhang, L. Ma, C. Qian, S. Zhou, C. Liang, M. Ling, Oxygen-coordinated low-nucleus cluster catalysts for enhanced electrocatalytic water oxidation, Carbon Energy 5 (2023) e216, https://doi.org/10.1002/cey2.216.

[56] R. Yao, Y. Wu, K. Zhang, S. Fan, Q. Zhao, J. Li, G. Liu, Lattice strain induced by trace pt single atoms in nickel for accelerating industrial hydrogen evolution, J. Energy Chem. 98 (2024) 503–511, https://doi.org/10.1016/j.jechem.2024.07.020.

[57] J. Li, C. Zhang, T. Zhang, Z. Shen, Q. Zhou, J. Pu, H. Ma, T. Wang, H. Zhang, H. Fan, Y. Wang, H. Ma, Multiple-interface relay catalysis: enhancing alkaline hydrogen evolution through a combination of volmer promoter and electrical-behavior regulation, Chem. Eng. J. 397 (2020) 125457, https://doi.org/10.1016/j.cej.2020.125457.

[58] J. Shen, M. Zhang, Y. Huang, C. Chen, Y. Zheng, S. Dong, J. Jiang, W. Lei, S. Wang, H. Shao, Ru-induced lattice expansion of metallic co with favorable surface property for high-efficiency water electrolysis, Appl. Catal. B Environ. Energy 358 (2024) 124392, https://doi.org/10.1016/j.apcatb.2024.124392.

[59] J. Zhang, J. Liang, B. Mei, K. Lan, L. Zu, T. Zhao, Y. Ma, Y. Chen, Z. Lv, Y. Yang, C. Yu, Z. Xu, B.Y. Xia, W. Li, Q. Yuan, D. Zhao, Synthesis of Ni/NiO@MoO_{3-x} composite nanoarrays for high current density hydrogen evolution reaction, Adv. Energy Mater. 12 (2022) 2200001, https://doi.org/10.1002/aenm.202200001.

[60] D. Jin, F. Qiao, Y. Zhou, J. Wang, K. Cao, J. Yang, J. Zhao, L. Zhou, H. Li, Cu/Mo_2C synthesized through Anderson-type polyoxometalates modulate interfacial water structure to achieve hydrogen evolution at high current density, Nano Res 17 (2024) 2546–2554, https://doi.org/10.1007/s12274-023-6237-6.

[61] X. Chen, X.-T. Wang, J.-B. Le, S.-M. Li, X. Wang, Y.-J. Zhang, P. Radjenovic, Y. Zhao, Y.-H. Wang, X.-M. Lin, J.-C. Dong, J.-F. Li, Revealing the role of interfacial water and key intermediates at ruthenium surfaces in the alkaline hydrogen evolution reaction, Nat. Commun. 14 (2023) 5289, https://doi.org/10.1038/s41467-023-41030-1.

[62] M.W. Louie, A.T. Bell, An investigation of thin-film Ni–Fe oxide catalysts for the electrochemical evolution of oxygen, J. Am. Chem. Soc. 135 (2013) 12329–12337, https://doi.org/10.1021/ja405351s.
[63] Q. Hu, K. Gao, X. Wang, H. Zheng, J. Cao, L. Mi, Q. Huo, H. Yang, J. Liu, C. He, Subnanometric ru clusters with upshifted *d* band center improve performance for alkaline hydrogen evolution reaction, Nat. Commun. 13 (2022) 3958, https://doi.org/10.1038/s41467-022-31660-2.
[64] Y. Liu, Q. Li, R. Si, G.D. Li, W. Li, D.P. Liu, D. Wang, L. Sun, Y. Zhang, X. Zou, Coupling sub-nanometric copper clusters with quasi-amorphous cobalt sulfide yields efficient and robust electrocatalysts for water splitting reaction, Adv. Mater. 29 (2017) 1606200, https://doi.org/10.1002/adma.201606200.